Alicia Arranz, Di Dong, Shouping Zhu, Markus Rudin, Christos Tsatsanis, Jie Tian, and Jorge Ripoll, "Helical optical projection tomography," Opt. Express 21, 25912-25925 (2013)

Helical optical projection tomography

Alicia Arranz,[1,8] Di Dong,[2,8] Shouping Zhu,[3] Markus Rudin,[1] Christos Tsatsanis,[4] Jie Tian[2,3] and Jorge Ripoll[5,6,7,*]

[1]*Institute for Biomedical Engineering, Swiss Federal Institute of Technology (ETH) Zurich, Wolfgang-Pauli-Strasse 10, 8093 Zurich, Switzerland*
[2]*Institute of Automation, Chinese Academy of Sciences, Beijing, 100190, China*
[3] *School of Life Sciences and Technology, Xidian University, Xian, Shaanxi 710071, China*
[4]*Laboratory of Clinical Chemistry, School of Medicine, University of Crete, Heraklion 71003, Greece*
[5] *Institute of Electronic Structure and Laser, Foundation for Research and Technology-Hellas (FORTH), 71110 Heraklion, Greece*
[6]*Department of Bioengineering and Aerospace Engineering, Universidad Carlos III of Madrid, 28911 Madrid, Spain*
[7]*Experimental Medicine and Surgery Unit, Instituto de Investigación Sanitaria del Hospital Gregorio Marañón, 28007 Madrid, Spain*
[8]*These authors have contributed equally to this work.*
[*]*jorge.ripoll@uc3m.es ;*

Abstract: A new technique termed Helical Optical Projection Tomography (hOPT) has been developed with the aim to overcome some of the limitations of current 3D optical imaging techniques. hOPT is based on Optical Projection Tomography (OPT) with the major difference that there is a translation of the sample in the vertical direction during the image acquisition process, requiring a new approach to image reconstruction. Contrary to OPT, hOPT makes possible to obtain 3D-optical images of intact long samples without imposing limits on the sample length. This has been tested using hOPT to image long murine tissue samples such as spinal cords and large intestines. Moreover, 3D-reconstructed images of the colon of DSS-treated mice, a model for Inflammatory Bowel Disease, allowed the identification of the structural alterations. Finally, the geometry of the hOPT device facilitates the addition of a Selective Plane Illumination Microscopy (SPIM) arm, providing the possibility of delivering high resolution images of selected areas together with complete volumetric information.

OCIS codes: (180.2520) Fluorescence microscopy; (180.6900) Three-dimensional microscopy; (170.3010) Image reconstruction techniques; (170.3660) Light propagation in tissues.

References and links

1. V. Ntziachristos, "Going deeper than microscopy: the optical imaging frontier in biology," Nat. Methods **7**(8), 603–614 (2010).
2. J. Sharpe, U. Ahlgren, P. Perry, B. Hill, A. Ross, J. Hecksher-Sørensen, R. Baldock, and D. Davidson, "Optical projection tomography as a tool for 3D microscopy and gene expression studies," Science **296**(5567), 541–545 (2002).
3. J.-F. Colas and J. Sharpe, "Live optical projection tomography," Organogenesis **5**(4), 211–216 (2009).
4. J. Huisken, J. Swoger, F. Del Bene, J. Wittbrodt, and E. H. Stelzer, "Optical sectioning deep inside live embryos by selective plane illumination microscopy," Science **305**(5686), 1007–1009 (2004).
5. P. J. Keller, A. D. Schmidt, A. Santella, K. Khairy, Z. Bao, J. Wittbrodt, and E. H. K. Stelzer, "Fast, high-contrast imaging of animal development with scanned light sheet-based structured-illumination microscopy," Nat. Methods **7**(8), 637–642 (2010).
6. S. Preibisch, S. Saalfeld, J. Schindelin, and P. Tomancak, "Software for bead-based registration of selective plane illumination microscopy data," Nat. Methods **7**(6), 418–419 (2010).
7. P. J. Verveer, J. Swoger, F. Pampaloni, K. Greger, M. Marcello, and E. H. K. Stelzer, "High-resolution three-dimensional imaging of large specimens with light sheet-based microscopy," Nat. Methods **4**(4), 311–313 (2007).
8. T. V. Truong, W. Supatto, D. S. Koos, J. M. Choi, and S. E. Fraser, "Deep and fast live imaging with two-photon scanned light-sheet microscopy," Nat. Methods **8**(9), 757–760 (2011).
9. M. B. Ahrens, M. B. Orger, D. N. Robson, J. M. Li, and P. J. Keller, "Whole-brain functional imaging at cellular resolution using light-sheet microscopy," Nat. Methods **10**(5), 413–420 (2013).

#193656 - $15.00 USD Received 10 Jul 2013; revised 5 Sep 2013; accepted 9 Sep 2013; published 23 Oct 2013

10. L. Gao, L. Shao, C. D. Higgins, J. S. Poulton, M. Peifer, M. W. Davidson, X. Wu, B. Goldstein, and E. Betzig, "Noninvasive imaging beyond the diffraction limit of 3D dynamics in thickly fluorescent specimens," Cell **151**(6), 1370–1385 (2012).
11. H.-U. Dodt, U. Leischner, A. Schierloh, N. Jährling, C. P. Mauch, K. Deininger, J. M. Deussing, M. Eder, W. Zieglgänsberger, and K. Becker, "Ultramicroscopy: three-dimensional visualization of neuronal networks in the whole mouse brain," Nat. Methods **4**(4), 331–336 (2007).
12. A. Ertürk, C. P. Mauch, F. Hellal, F. Förstner, T. Keck, K. Becker, N. Jährling, H. Steffens, M. Richter, M. Hübener, E. Kramer, F. Kirchhoff, H. U. Dodt, and F. Bradke, "Three-dimensional imaging of the unsectioned adult spinal cord to assess axon regeneration and glial responses after injury," Nat. Med. **18**(1), 166–171 (2011).
13. H. Siedentopf and R. Zsigmondy, "Uber Sichtbarmachung und Größenbestimmung ultramikoskopischer Teilchen, mit besonderer Anwendung auf Goldrubingläser," Ann. Phys. **315**(1), 1–39 (1902).
14. M. Rudin, *Molecular Imaging: Basic Principles and Applications in Biomedical Research*, 1st Edition (Imperial College Press, 2005), p. 540.
15. J. B. Pawley, *Handbook of Biological Confocal Microscopy* (Plenum Press, 1995).
16. M. Rieckher, U. J. Birk, H. Meyer, J. Ripoll, and N. Tavernarakis, "Microscopic optical projection tomography in vivo," PLoS ONE **6**(4), e18963 (2011).
17. C. Vinegoni, C. Pitsouli, D. Razansky, N. Perrimon, and V. Ntziachristos, "In vivo imaging of Drosophila melanogaster pupae with mesoscopic fluorescence tomography," Nat. Methods **5**(1), 45–47 (2007).
18. L. McGurk, H. Morrison, L. P. Keegan, J. Sharpe, and M. A. O'Connell, "Three-dimensional imaging of Drosophila melanogaster," PLoS ONE **2**(9), e834 (2007).
19. U. J. Birk, A. Darrell, N. Konstantinides, A. Sarasa-Renedo, and J. Ripoll, "Improved reconstructions and generalized filtered back projection for optical projection tomography," Appl. Opt. **50**(4), 392–398 (2011).
20. A. Bassi, L. Fieramonti, C. D'Andrea, M. Mione, and G. Valentini, "In vivo label-free three-dimensional imaging of zebrafish vasculature with optical projection tomography," J. Biomed. Opt. **16**(10), 100502 (2011).
21. R. J. Bryson-Richardson and P. D. Currie, "Optical projection tomography for spatio-temporal analysis in the zebrafish," Methods Cell Biol. **76**, 37–50 (2004).
22. L. Fieramonti, A. Bassi, E. A. Foglia, A. Pistocchi, C. D'Andrea, G. Valentini, R. Cubeddu, S. De Silvestri, G. Cerullo, and F. Cotelli, "Time-gated optical projection tomography allows visualization of adult zebrafish internal structures," PLoS ONE **7**(11), e50744 (2012).
23. J. Swoger, M. Muzzopappa, H. López-Schier, and J. Sharpe, "4D retrospective lineage tracing using SPIM for zebrafish organogenesis studies," J. Biophotonics **13**, 1–13 (2010).
24. T. Alanentalo, A. Asayesh, H. Morrison, C. E. Lorén, D. Holmberg, J. Sharpe, and U. Ahlgren, "Tomographic molecular imaging and 3D quantification within adult mouse organs," Nat. Methods **4**(1), 31–33 (2007).
25. V. Kumar, E. Scandella, R. Danuser, L. Onder, M. Nitschké, Y. Fukui, C. Halin, B. Ludewig, and J. V. Stein, "Global lymphoid tissue remodeling during a viral infection is orchestrated by a B cell-lymphotoxin-dependent pathway," Blood **115**(23), 4725–4733 (2010).
26. C. Vinegoni, D. Razansky, J.-L. Figueiredo, L. Fexon, M. Pivovarov, M. Nahrendorf, V. Ntziachristos, and R. Weissleder, "Born normalization for fluorescence optical projection tomography for whole heart imaging," J. Vis. Exp. **28**(28), 1389 (2009).
27. K. Lee, J. Avondo, H. Morrison, L. Blot, M. Stark, J. Sharpe, A. Bangham, and E. Coen, "Visualizing Plant Development and Gene Expression in Three Dimensions Using Optical Projection Tomography," Plant Cell **18**(9), 2145–2156 (2006).
28. A. D. Leeper, J. Farrell, J. M. Dixon, S. E. Wedden, D. J. Harrison, and E. Katz, "Long-term culture of human breast cancer specimens and their analysis using optical projection tomography," J. Vis. Exp. **53**(53), 3085 (2011).
29. A. Kokolakis, G. Zacharakis, K. Krasagakis, K. Lasithiotakis, R. Favicchio, G. Spiliopoulos, E. Giannikaki, J. Ripoll, and A. Tosca, "Prehistological evaluation of benign and malignant pigmented skin lesions with optical computed tomography," J. Biomed. Opt. **17**(6), 066004 (2012).
30. A. Paradisi, C. Maisse, M.-M. Coissieux, N. Gadot, F. Lépinasse, C. Delloye-Bourgeois, J.-G. Delcros, M. Svrcek, C. Neufert, J.-F. Fléjou, J.-Y. Scoazec, and P. Mehlen, "Netrin-1 up-regulation in inflammatory bowel diseases is required for colorectal cancer progression," Proc. Natl. Acad. Sci. U.S.A. **106**(40), 17146–17151 (2009).
31. A. Arranz, C. Doxaki, E. Vergadi, Y. Martinez de la Torre, K. Vaporidi, E. D. Lagoudaki, E. Ieronymaki, A. Androulidaki, M. Venihaki, A. N. Margioris, E. N. Stathopoulos, P. N. Tsichlis, and C. Tsatsanis, "Akt1 and Akt2 protein kinases differentially contribute to macrophage polarization," Proc. Natl. Acad. Sci. U.S.A. **109**(24), 9517–9522 (2012).
32. A. Arranz, C. Reinsch, K. A. Papadakis, A. Dieckmann, U. Rauchhaus, A. Androulidaki, V. Zacharioudaki, A. N. Margioris, C. Tsatsanis, and S. Panzner, "Treatment of experimental murine colitis with CD40 antisense oligonucleotides delivered in amphoteric liposomes," J. Control. Release **165**(3), 163–172 (2013).
33. A. C. Kak and M. Slaney, *Principles of Computerized Tomographic Imaging* (IEEE Press, 1988).
34. S. Wirtz, C. Neufert, B. Weigmann, and M. F. Neurath, "Chemically induced mouse models of intestinal inflammation," Nat. Protoc. **2**(3), 541–546 (2007).
35. U. J. Birk, A. Darrell, N. Konstantinides, A. Sarasa-Renedo, and J. Ripoll, "Improved reconstructions and generalized filtered back projection for optical projection tomography," Appl. Opt. **50**(4), 392–398 (2011).
36. D. Dong, S. Zhu, C. Qin, V. Kumar, J. V Stein, S. Oehler, C. Savakis, J. Tian, and J. Ripoll, "Automated Recovery of the Center of Rotation in Optical Projection Tomography in the Presence of Scattering," IEEE Trans. Inf. Technol. Biomed. **17**, 198–204 (2012).

#193656 - $15.00 USD Received 10 Jul 2013; revised 5 Sep 2013; accepted 9 Sep 2013; published 23 Oct 2013

37. S. Zhu, D. Dong, U. J. Birk, M. Rieckher, N. Tavernarakis, X. Qu, J. Liang, J. Tian, and J. Ripoll, "Automated motion correction for in vivo optical projection tomography," IEEE Trans. Med. Imaging **31**(7), 1358–1371 (2012).
38. J. R. Walls, J. G. Sled, J. Sharpe, and R. M. Henkelman, "Resolution improvement in emission optical projection tomography," Phys. Med. Biol. **52**(10), 2775–2790 (2007).
39. L. Chen, J. McGinty, H. B. Taylor, L. Bugeon, J. R. Lamb, M. J. Dallman, and P. M. W. French, "Incorporation of an experimentally determined MTF for spatial frequency filtering and deconvolution during optical projection tomography reconstruction," Opt. Express **20**(7), 7323–7337 (2012).
40. J. R. Walls, J. G. Sled, J. Sharpe, and R. M. Henkelman, "Correction of artefacts in optical projection tomography," Phys. Med. Biol. **50**(19), 4645–4665 (2005).
41. Y.-Y. Fu, C.-W. Lin, G. Enikolopov, E. Sibley, A.-S. Chiang, and S.-C. Tang, "Microtome-free 3-dimensional confocal imaging method for visualization of mouse intestine with subcellular-level resolution," Gastroenterology **137**(2), 453–465 (2009).

1. Introduction

There has been considerable interest during this past decade on high resolution 3D optical imaging of intact samples and a host of techniques have been developed for this purpose [1]. Amongst them, Optical Projection Tomography (OPT) [2,3] – which uses angular measurements to recover the 3D structure in a manner analogous to X-ray computed tomography – and light sheet techniques such as Selective Plane Illumination Microscopy (SPIM) [4–10] or Ultramicroscopy [11–13]– which measure the fluorescence emission directly at a plane within the (non-scattering) sample – are the most commonly used when imaging *in-toto*. The technique we present here, helical Optical Projection Tomography (hOPT) is based on OPT with the significant difference that there is a translation of the sample in the vertical direction during the acquisition process. This requires adjusting the setup correspondingly and, most importantly, the development of new algorithms that will recover the 3D structure of the sample under these conditions.

OPT was developed in 2002 [2] as the tool able to fill the gap between Magnetic Resonance Imaging (MRI) [14] and Confocal Microscopy [15] when imaging samples from 1 to 10 mm across. Since then, OPT has been applied to image in 3D a wide range of samples with different applications. Gene expression studies have been performed in the mouse embryo [2] and *Caenorhabditis elegans* [16]; observation of internal structures have been possible in adult *Drosophila melanogaster* [17,18], *Parhyale hawaiensis* [19] and *Danio rerio*, which has also been used to obtain flow maps to reconstruct sections of the circulatory system [20–23]. OPT has also been applied to image fixed and cleared adult mouse organs [24–26] and different stages of plant development [27]. Its great potential has been tested with human samples and has been used for imaging and characterization of breast cancer biopsies [28] and melanoma [29]. More accurate modeling of light propagation using the same geometry as OPT has also been used for time-lapse imaging of *D. melanogaster* [17], and time-lapse imaging of limb-bud development has been shown under appropriate culture conditions [3]. Recently, time-gated OPT has also been proven capable of imaging scattering specimens such as adult zebrafish *in-vivo* by temporally selecting early-arriving light [22].

One of the main advantages of OPT is the possibility to obtain 3D images of intact samples with no upper limit on the size, as long as the imaging system can accommodate the sample in its field of view while keeping it in focus. The only physical limitation is the amount of scattering present in the sample, which is either: a) removed by fixing and clearing the tissues [25]; b) partially avoided through time-gating techniques [22]); or c) modeled and accounted for to some extent [17]. However, if one of the dimensions of the sample greatly exceeds the other two, i.e. we are dealing with very long samples, we need to resort to imaging the sample in sections. Thus, sample segmentation and/or repeated overlapping measurements followed with post-acquisition analysis ('stitching') were until now the only possible solution to this drawback. Data 'stitching', however, also implies longer measurement times, extended light-exposures of the sample, and uneven photobleaching. As will be shown later, the uneven photobleaching due to 'stitching' may result in 3D reconstructions with very strong variations on image intensity.

#193656 - $15.00 USD Received 10 Jul 2013; revised 5 Sep 2013; accepted 9 Sep 2013; published 23 Oct 2013

Under these circumstances, long samples with high biological interest such as mouse spinal cord, long bones, colon or small intestine, amongst others, have to be segmented prior to imaging [12]. Up to date, it has therefore been very difficult to image long samples *in-toto* with the existing techniques (for a review on existing techniques see [1]; for a comparison of SPIM with confocal see [7] or [10]). Long samples such as the ones described above are of great significance in current biomedical research topics such as intestinal carcinogenesis [30], inflammatory bowel diseases [31,32], multiple sclerosis [12], and many others. With these applications in mind, the aim of this work was to develop a system that would overcome the sample-length limitation of OPT while ensuring the sample is homogeneously exposed to light. As a result, we present helical-OPT (hOPT), a new approach for 3D optical imaging of very long samples. hOPT consists of vertically displacing the sample while simultaneously rotating it during the acquisition process, in a manner analogous to spiral or helical X-ray computed tomography [33]. This rotation-translation movement is later on accounted for when applying the inverse Radon transform, the mathematical expression which maps the measurements taken at different angles onto a 3D image (see [33] for a thorough description on the methodology). The incorporation of a SPIM arm in the hOPT set-up allowed the acquisition of high resolution images of selected areas of the samples, which also served as validation of the 3D reconstructed data obtained with hOPT.

This paper is structured as follows: in section 2 we present details on the materials and methods, in particular on the setup and sample preparation. Section 3 presents a numerical simulation to showcase the benefits of hOPT over conventional "stitched" OPT, and results of hOPT applied to murine tissues. Finally Sections 4 and 5 present the discussion and conclusions.

2. Materials and methods

2.1 Set-up description

Figures 1(a)-1(c) depict all components of the hOPT setup, including the rotation/translation stages, with the sample (S) placed in a bath of BABB (benzyl alcohol and benzyl benzoate in a 1:2 ratio) – when required – (B), an excitation and white light reference light emitting diode (LED1 and LED2, respectively; Luxeon V Star, Philips Lumileds Lighting, San Jose, California), the detection objective (OLd) and tube lens (TL) assembly featuring an emission filter (Fd) and an iris diaphragm (I), and an EMCCD camera (iXon DV885, Andor Corp, Belfast, Northern Ireland, with 13μm x 13μm physical detector size and a 1004 x 1002 sensor; a 2 x 2 binning was used throughout the experiments) thermoelectrically cooled to -70^{o}C. The fluorescence excitation light (LED1) is roughly collimated and its spectrum narrowed by an excitation filter (Fi) centered at 488nm, whereas the white light (LED2) for trans-illumination passes through a ground glass diffuser (D) (note that the while light illumination component is only shown in Fig. 1(c). The whole setup is assembled on an optical table (Vere, New Kensinton, U.S.A.) with a passive vibration isolation system.

The SPIM arm consisted on a 473nm 100mW laser (Roithner LaserTechnik, Vienna, Austria), directed through mirrors (M) towards the illumination objective (OLi) after passing through a cylindrical lens (CL) of focal length f = 10mm. A detailed close-up of the movement and rotation stages together with the glass cuvette is shown in Fig. 1(d). Depending on the fluorophores used, appropriate light sources (and filters) can be automatically selected. For all SPIM measurements shown here the detection optics consisted of an infinity corrected 20x long-working distance objective (Mitutoyo, Kawasaki, Japan) with numerical aperture (NA) 0.42, working distance (WD) 20mm and depth of focus (DF) 1.6μm. The SPIM illumination objective was an infinity corrected 10x long-working distance objective (Mitutoyo, Kawasaki, Japan; NA 0.28, WD 33.5mm, DF 3.5μm), generating a light sheet thickness of approximately 2.5μm. The total SPIM imaging system in this configuration offers a resolution of approximately ~2.5μm in the optical axis (z) and ~1.7μm in the image plane (xy), for a Field of View (FOV) of 0.87mm.

#193656 - $15.00 USD Received 10 Jul 2013; revised 5 Sep 2013; accepted 9 Sep 2013; published 23 Oct 2013

In the case of hOPT, detection was performed using either a 2.5x Infinity Acrovid microscope objective (Infinity, Boulder, U.S.A; NA 0.064, WD 37.0mm and DF 75.0µm), or a 5x long-working distance objective (Mitutoyo, Kawasaki, Japan; NA 0.14, WD 34mm and DF 14µm). The 2.5x and 5x objectives present an isotropic resolution of approximately 13.2µm and 7.6µm, each covering a FOV of 6.6mm and 3.8mm, respectively. All hOPT measurements presented here were taken with the 5x objective.

Depending on the emission characteristics of the fluorophore or fluorescent protein used, the detection filter (Fd) was either a 531 ± 40nm bandpass filter (Semrock, Rocherster, NY) appropriate for GFP and AF488-Phalloidin or a 605 ± 70nm bandpass filter (Chroma, Bellows Falls, VT), appropriate for propidum iodide. Exposure times in both SPIM and hOPT modalities were similar when imaging the same sample, with values in the range of 0.02s. The overall duration of the experiment depended on the length of the sample, for example requiring 500 SPIM measurements to cover a volume of 0.87x0.87x1.25mm and 3875 hOPT measurements to cover a volume of 3.8x50x3.8mm (i.e. a volume roughly 760 times larger). Approximate experimental times for these volumes where 25s and 200s, respectively, including motor movement and data transfer.

Sample movement was controlled with three translation stages (8MT167-100, Standa, Vilnius, Lithuania) and one rotation stage (8MR190-2, Standa, Vilnius, Lithuania) with the requisite that at least the y-stage has a long travel range (our linear stages had a travel range of 10cm). In order to image large samples a bath with dimensions such that the complete sample could rotate freely was used. In our case, we used a glass bath made of crown glass (MultiLab Ltd, Newcastle Upon Tyne, UK), with dimensions 80x30x30 mm, wall thickness 1.25mm and index of refraction 1.52.

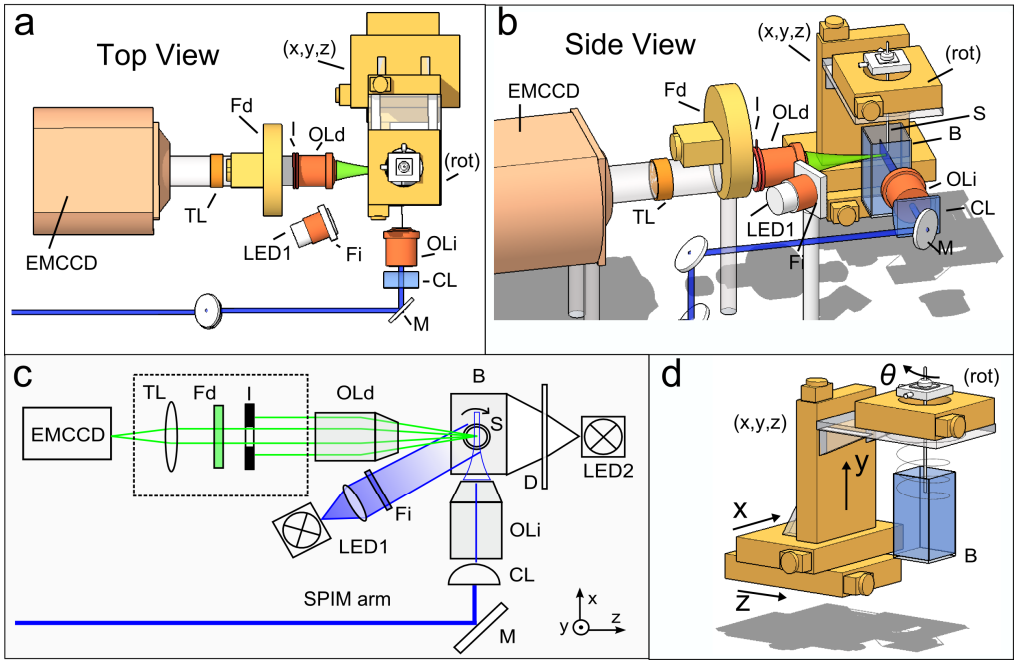

Fig. 1. Description of the hOPT set-up (a, b and c), its main components consisting of a detection objective (OLd), a tube lens (TL), an emission filter (Fd), an iris (I) which is projected to an EMCCD camera, an excitation source (LED1) and an excitation filter (Fi) and a white light (LED2) with a diffusor (D). Note that for simplicity LED2 has not been included in (a) and (b), its position being behind the bath (B) as shown in (c). The SPIM arm consists of a 473nm laser, mirrors (M), a cylindrical lens (CL) and an excitation objective (OLi). The rotation/translation module enables simultaneous rotation and translation (d). When required, samples (S) were imaged in a BABB bath (B). More details about the description of the set-up can be found in Section 2.1.

#193656 - $15.00 USD Received 10 Jul 2013; revised 5 Sep 2013; accepted 9 Sep 2013; published 23 Oct 2013

2.2 Sample preparation

All procedures described here were approved by the Zurich Cantonal Veterinary Office (Zurich, Switzerland) or by the Veterinary Department of the Heraklion Prefecture (Heraklion, Crete, Greece). Mice were housed at the animal facility in the Animal Imaging Center, ETH-Zurich or at the animal facility in the School of Medicine, University of Crete. Animals were kept at standard housing conditions providing water and food *ad libitum*. The dextran sodium sulphate (DSS) model use for the inflammation-derived alteration study was established as described previously [34]. Briefly, age-matched C57BL/6 mice received 3.5% weight/vol DSS (36–50 kDa, MP Biomedicals) in the drinking water for 5 days followed by 3 days of autoclaved water administration. Model development was followed up by measuring weight loss daily.

Prior collection of tissue samples, animals were deeply anesthetized and euthanized. Tissues (colons, small intestines and spinal cords) were aseptically removed, washed with PBS (colons and small intestines were also flushed with PBS) and fixed in 4% PFA for at least 24h at 4°C. After fixation, samples were washed twice with PBS, incubated with 1% weight/vol Triton X-100 for 30 minutes and washed again with PBS prior to staining. Single staining with propidium iodide (30μg/ml in PBS; Sigma-Aldrich, St. Louis, MO) was performed at room temperature for 30 minutes in the dark followed by three washes with PBS of 10 minutes each. When double staining was performed, samples were incubated with Alexa-Fluor 488 Phalloidin (100 units; Molecular Probes, Invitrogen, US) for 1 hour at room temperature and in the dark, washed three times with PBS for 10 minutes and then incubated with propidium iodide as described above.

Once the staining procedure was completed, samples were mounted in 1.3% low-melting agarose (SeaPlaque, Lonza Rockland Inc, Rockland, ME). Mounted samples were then dehydrated by successive washes through a graded series of methanol (25%, 50%, 75% and 100%; 1 hour per wash) and left in 100% methanol overnight. Mounted samples were then transferred to BABB (benzyl alcohol and benzyl benzoate in a 1:2 ratio; Sigma-Aldrich, St. Louis, MO) for at least 24 hours. Whenever imaging tissue samples, measurements were performed with the samples submerged in BABB.

2.3 Acquisition procedure

Samples are mounted and attached to a rotation/translation platform which allows precise positioning of the sample in three dimensions using customized software. hOPT images were acquired by adjusting the speed of the vertical translation (v_y) and rotation (v_{rot}). These values were set based on the exposure time needed for each sample so that a full 360° rotation took place before the lower point in the image reached the top of the field of view. This is done to ensure that the reconstruction algorithm has sufficient projections to render a good quality image. Additionally, this approach enables the use of video-rate imaging while moving the stages at a constant speed, instead of the move-and-acquire approach typically used in OPT. Even though our system can achieve frame rates of 100 frames per second, in order to optimize the signal to noise ratio the frame speeds used in the measurements shown here were in the order of 30 frames per second (video-rate). Using video-rate imaging with a highly sensitive CCD camera minimizes the time required for imaging large samples and therefore reduces photobleaching and phototoxic effects, which are very significant particularly when dealing with live samples. We thus optimized the number of images acquired per full rotation by tuning both the exposure time (to ensure high signal to noise ratio) and the speeds, taking into account that they are related as:

$$v_{\mathrm{rot}} \le \frac{2\pi}{T_{\mathrm{exp}} N_{rot}^{\min}}, \quad (rad/s) \tag{1}$$

$$v_{\mathrm{y}} \le \frac{FOV_{y}}{T_{\mathrm{exp}} N_{rot}^{\min}}, \quad (mm/s) \tag{2}$$

#193656 - $15.00 USD Received 10 Jul 2013; revised 5 Sep 2013; accepted 9 Sep 2013; published 23 Oct 2013

In the above relations FOV_y represents the y-dimension of the field of view, $T_{\exp}$ is the exposure time and $N_{rot}^{\min}$ being the minimum number of projections needed for the reconstruction algorithm. The procedure for finding the optimal values of v_{rot}, v_y and $T_{\exp}$ is to first find the minimum value of the exposure time which still gives a good signal to noise ratio. In the examples shown here, $N_{rot}^{\min}$ was set to 500. Once the optimum speeds and exposure times are found, they do not need to be changed as long as the field of view is maintained and the emission intensity of the samples is comparable.

During data acquisition each measurement is saved onto a tiff-stack, with the important feature that all the information with respect to the stages (x, y, z and rotation) is included, together with a time-stamp. This enables our reconstruction code to identify the actual speeds in order to transform our data into regular OPT data which can be fed to a reconstruction algorithm.

As mentioned previously, our hOPT setup is fitted with a SPIM illumination arm using a laser, a cylindrical lens and a microscope objective [4,23]. This permits both light-sheet and hOPT measurements to be acquired on the same system and without interacting with the sample. hOPT offers the fast representation of a lower resolution 3D volume (~7.6μm in this specific case) of the complete sample while SPIM delivers higher resolution images (the SPIM lateral resolution in the configuration presented here is ~1.7μm). This is mainly due to the different needs regarding the depth of focus of each technique: OPT relies on large depths of field so that the sample remains in focus while rotating; on the other hand, SPIM generates optimal images when the depth of field is as narrow as possible. This important difference is what makes their combination in a single setup a very useful one, since in this way we can perform first a lower resolution hOPT of the full sample and then select those areas of interest which we may then image with higher resolution using SPIM. Note that one of the requisites for this is a quasi-real time reconstruction scheme, which in our case was implemented using Graphics Processing Units (GPUs, see below). Even though the SPIM measurements shown here were obtained for a single angle, it is straightforward to implement a multiple angle SPIM approach as shown in [6].

2.4 Fast reconstruction method

The reconstruction method consisted of three main steps: 1) reading and transforming data into xy vs. rotation data; 2) automatic search of the center of rotation; and 3) implementation of the Filtered Back-Projection (FBP) algorithm [33] to solve the inverse Radon transform. Since this is an extremely computing intensive process, all steps were programmed in CUDA and executed using a Graphics Processing Unit (GPU) using a desktop computer running on 64-bit Windows 7, with an Intel Core2 2.66 GHz CPU, a 2GB DDR2 RAM, and a NVIDIA GTX 275 GPU card containing an 896MB device memory. This implementation in a parallel environment enabled 3D reconstructions to be obtained in a matter of seconds. Step 1 consisted of building the sinogram (a matrix representing the intensity for each line of pixels versus the projection angle) for each veritical position of the sample. This is done by choosing the appropriate lines of pixels in the measurements once we have accounted for the speed of vertical displacement. In Step 2 we made use of an automatic search for the center of rotation consisting on maximizing the variance of the reconstructed image, performing first a coarse search and then a fine search. Details of the automatic search for the center of rotation can be found in [35–37]. Once the center of rotation was found, the FBP algorithm [33] with the new estimated center of rotation was implemented optimizing the reconstruction speed using GPUs, as previously described [36]. Whenever the sample's width span was greater than the field of view, the hOPT data was built by combining two views with a slight x-displacement in order to make sure the sample was always within the field of view while completing the full 360° rotation.

In all the hOPT reconstructions presented in this work we have made use of a standard FBP algorithm. There are, however, other more advanced procedures that would increase the

#193656 - $15.00 USD Received 10 Jul 2013; revised 5 Sep 2013; accepted 9 Sep 2013; published 23 Oct 2013

resolution of the resulting image, such as those shown in [38,39], for example. We would like to point out that all improved reconstruction procedures from which OPT can benefit may also be applied to hOPT.

3. Results

3.1 Advantages of helical OPT over stitched-OPT

One of the most significant advantages of helical OPT over stitching sequential sections of OPT data is the fact that photobleaching is not only reduced but that it affects homogeneously the whole sample. In order to illustrate this point when imaging a sample which exceeds the field of view (FOV) of the setup, we have performed the following numerical simulation: a homogeneous fluorescent cylinder of L/5 in diameter and height 4L is imaged both by hOPT and OPT through a FOV of LxL (see Fig. 2(a)). For the numerical simulation we used L = 20mm, with sampling detectors of 0.1mm yielding a FOV of 200x200 pixels, and 360 angular measurements. In the hOPT simulation we assume that the sample rotates while it is displaced vertically in such a way that when it has completed a full rotation it has advanced L in the y axis. On the other hand, when imaging the same long sample with OPT, in order to stitch the fields of view together, we need significant overlap to enable accurate stitching. To that end, three different overlaps are considered, namely 10%, 25% and 50% of the FOV. To study the effect of photobleaching we first considered the scenario where photobleaching is negligible. Results for this case are portrayed in Fig. 2(b), where both hOPT and OPT will produce identical images, with OPT needing longer acquisition and reconstruction times proportionally to the amount of overlap (see Table 1). As a second case scenario, following [40] we introduced in our simulation 20% of photobleaching after the completion of a full 360° rotation. Since the amount of photobleaching is proportional to the number of angular measurements, we will for example bleach 20% of the signal after 360° and up to 40% in those areas which need to be exposed twice, such as the overlapping regions. Expressed in terms of the intensity of the reconstructed image, I, this can be expressed as $I(\theta) = I_0 - I_0 \frac{\Phi}{2\pi}\theta$, with I_0 representing the un-bleached intensity, Φ the amount of photobleaching per full rotation (0.2 in the case presented here), and θ the angular measurement. The integrated mean of this equation over 2π, $\langle I \rangle = \frac{1}{2\pi}\int_0^{2\pi} I(\theta) d\theta$, yields $\langle I \rangle = I_0 (1 - \Phi/2)$.

Results for helical OPT are shown in Fig. 2(b), while OPT results with 10%, 25% and 50% overlap are shown in Fig. 2(c), 2(d), and 2(e). As can be seen in Fig. 2(b), hOPT exposes homogeneously the whole sample, rendering an image which has its intensity reduced in 10% ($\langle I \rangle = I_0 (1 - \Phi/2) = 0.9 I_0$). On the other hand, when stitching OPT images those areas which have been exposed twice will suffer double amount of bleaching, resulting in a 20% reduction of the reconstructed intensity as shown in Figs. 2(c), 2(d) and 2(e). For completion, a plot through the axis of the reconstructed cylinder is shown in Fig. 2(f), where we can see how stitching affects the reconstructed data. As expected, a 50% overlap produces a homogeneous image since all areas are exposed twice, at the significant expense of reconstruction and acquisition times and more importantly, extended exposures. Note that the 50% overlap would need to acquire an extra OPT data set (8 sections to be stitched, instead of the 7 used here) if the complete cylinder needs to be illuminated homogeneously, hence the results in Fig. 2(e) which show a region of lower photobleaching at the top.

To showcase the increase in reconstruction and acquisition times due to the overlapping regions, we calculated the increase in exposure time and computation time incurred in the results presented in Fig. 2. Results are shown in Table 1 where, as expected, both acquisition and reconstruction times increase linearly with the size of the overlapped region. Reconstruction times include reading data from disk to memory, reconstructing this data

#193656 - $15.00 USD Received 10 Jul 2013; revised 5 Sep 2013; accepted 9 Sep 2013; published 23 Oct 2013

using GPUs, and saving the results to disk. Acquisition times are measured with the hOPT acquisition time as a reference but neglecting the amount of time needed to displace the sample, which would significantly increase the overall time of the experiment. As mentioned previously, the 50% overlap for the case studied here needs 7 field of views instead of 8 to cover the full height of the cylinder (h = 4L). This explains the fact that the total acquisition time shown in Table 1 is 1 + 7/8 = 1.875 times higher than the acquisition time in the hOPT case. However, note that in this way half of the last section covered will have been exposed only once, as can be seen in Fig. 2(e).

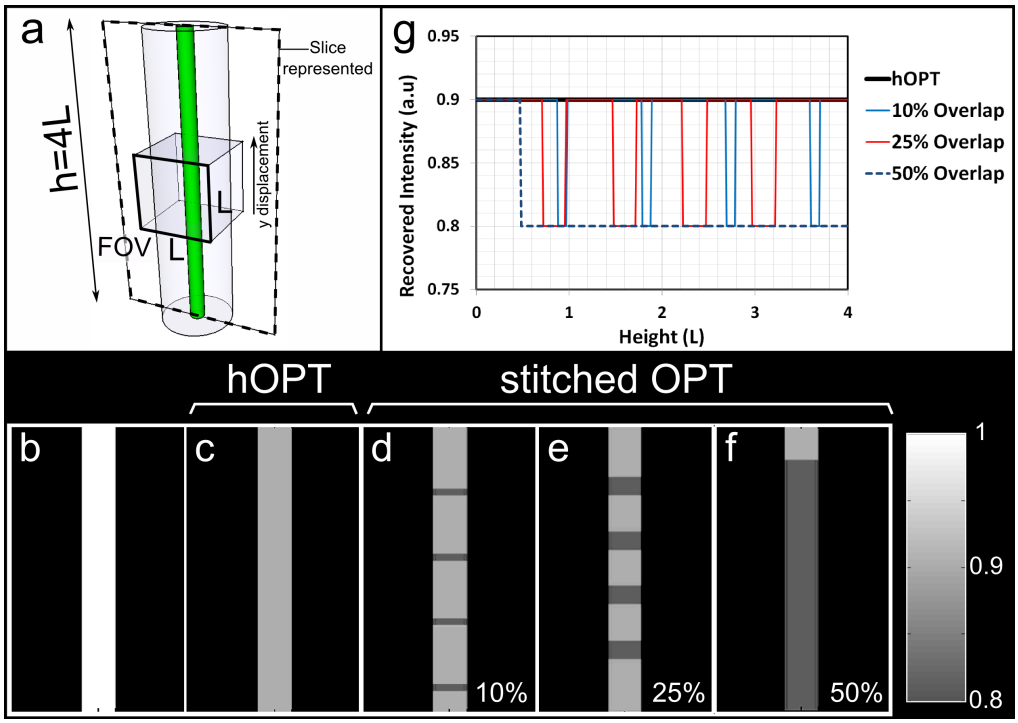

Fig. 2. In order to compare hOPT with the results obtained by stitching OPT segments, a numerical simulation was performed considering a fluorescent cylinder of L/5 diameter and 4L in height as test object, as shown in (a), using a field of view of LxL. (b) Results for hOPT and stitched-OPT for the case of no photobleaching. (c) Results for hOPT for linear photobleaching of 20% per full rotation. (d), (e) and (f) Results for stitched-OPT with 10%, 25% and 50% overlap, respectively, for a linear photobleaching of 20% per full rotation. (g) Plots through the axis of the cylinder for the cases shown in (c)-(f).

Table 1. Comparison of computation times

	hOPT	**Stitched-OPT**		
		10% overlap	**25% overlap**	**50% overlap**
Data Size	225,000 Kb	247,500 Kb	281.250Kb	421,875 Kb
Reconstruction Time	3.357s	3.663s	3.797s	4.434s
Rel. Acquisition Time*	1	>1.10	>1.25	>1.87
*Measurement times compared with hOPT, not accounting for time required for displacement				

3.2 hOPT enables 3D imaging of long samples

In order to analyze the performance of our approach, different tissue samples were prepared and imaged as described in Section 2. Figure 3(a) shows 3D images of the colon (approx. 55

#193656 - $15.00 USD Received 10 Jul 2013; revised 5 Sep 2013; accepted 9 Sep 2013; published 23 Oct 2013

mm long) of a 5 week-old female C57BL/6 mouse, stained with propidium iodide (nuclei) and AF488-Phalloidin (filamentous actin; see Sec. 2, Materials and Methods). The reconstructed images allow the observation of different sections of the colon from the cecum to the rectum (Fig. 3(ai)), with the corresponding differences in structure (note i.e. the transverse mucosal folds in the proximal colon, Fig. 3(aii) and 3(aiii)). Three selected areas of the same colon were also imaged in high resolution using the additional SPIM illumination arm (Fig. 3(a*iv*) and 3(a*v*) and Media 1). Using the volumetric stack of SPIM images, we obtained transversal views of the selected colon areas, which allowed us to validate the accuracy of the 3D reconstructed images obtained by hOPT, as shown in Fig. 3(aiii) and 3(a*iv*).

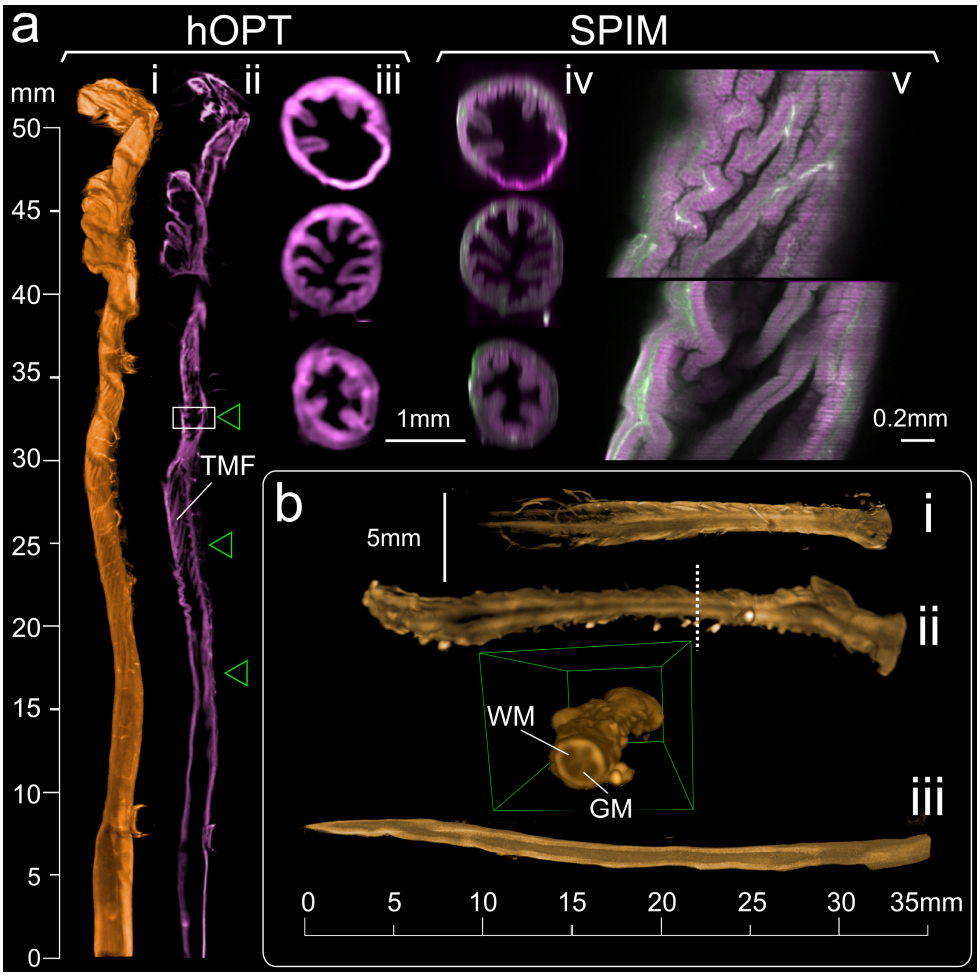

Fig. 3. Different samples were prepared and imaged as described in **Section 2** in order to test the performance of the hOPT system. a) Murine colon images: (i) Volume render generated from hOPT measurements. (ii) Longitudinal slice through the center of the volume, where the transverse mucosal folds (TMF) can be distinguished in the proximal colon. (iii) Transversal hOPT slices from the positions shown by green arrowheads. (iv) SPIM measurements from the same positions shown in (iii), validating the 3D reconstructed images obtained by hOPT (see full stack in Media 1). (v) SPIM measurements at two different depths of the area shown in the white box of (ii); in magenta, staining with propidium iodide and in green, staining with AF488 Phalloidin. b) Volume render generated from hOPT measurements of two mouse spinal cords (i) and (ii), showing below a transversal view of (ii), where the grey and white matters (GM and WM) can be distinguished. (iii) Shows a 35 mm piece of murine small intestine. (Media 1)

#193656 - $15.00 USD Received 10 Jul 2013; revised 5 Sep 2013; accepted 9 Sep 2013; published 23 Oct 2013

It must be stated at this point that a thorough comparison of the resolution of OPT and SPIM under similar detection conditions is lacking in the literature, and is out of the scope of this paper. The main difference between these two techniques relies on the fact that OPT (and therefore hOPT) requires most of the sample to be in focus, and thus needs large depths of field and low numerical apertures. SPIM on the other hand requires sharp focal planes and high numerical apertures. In this respect it is expected that SPIM will provide higher resolution than OPT in the imaging plane; however, since OPT (and hOPT) requires an inversion algorithm to provide a 3D image, it is possible to enhance the resolution during the reconstruction (see for example [38,39]). A comparison of SPIM and OPT is thus not straightforward.

Other examples of hOPT imaging of long samples are shown in Fig. 3(b), where two murine spinal cords – Fig. 3(bi) and 3(bii) - and a 3.5 cm long section of a mouse small intestine Fig. 3(biii) are presented. Transversal images of the 3D reconstructed data allowed us to distinguish different structures in the tissue samples such as white and grey matters in the spinal cords (Fig. 3(bii)).

A 3D section and volume render of a 20 mm long piece of small intestine containing a Peyer's Patch stained with propidium iodide are presented in Fig. 4(a) and 4(b), respectively, allowing the recognition of several B-cell follicles. The structure of the intestinal villi is also shown in Fig. 4(c) as well as a high resolution SPIM data of the same selected area (Fig. 4(d)). These results highlight the detailed anatomical information of the whole sample provided by hOPT in a quick and efficient manner which, if required, allows the selection of a specific area of interest that can be then imaged in higher resolution by SPIM. Note that imaging the complete volume of long samples such as these using SPIM even though feasible is unpractical due to the time it would require.

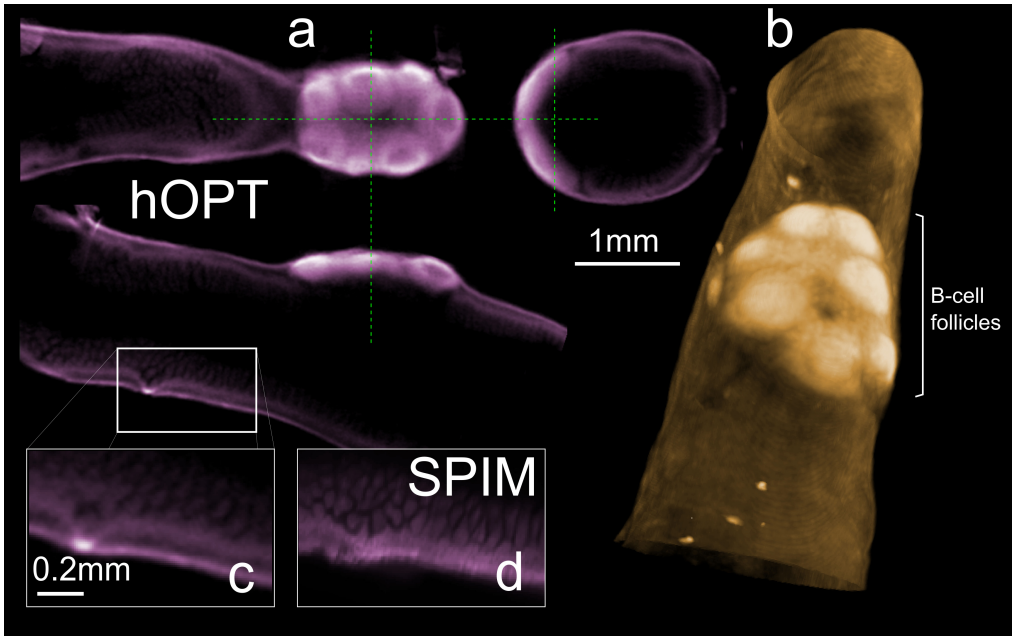

Fig. 4. A 20mm piece of a mouse small intestine containing a Peyer's Patch was obtained, stained, mounted and imaged as described in Materials and Methods. (a) Coronal, sagittal and transversal hOPT slices showing the B-cell follicles present in the Peyer's Patch. b) 3D volume render. (c) Details of the small intestine mucosa from a hOPT reconstruction compared to the same selected area imaged with SPIM (d).

#193656 - $15.00 USD Received 10 Jul 2013; revised 5 Sep 2013; accepted 9 Sep 2013; published 23 Oct 2013

3.3 Observation of inflammation-derived tissue alterations in colons from DSS-treated mice using hOPT

In order to test hOPT in more practical situations, we imaged colons from both healthy and dextran sodium sulphate (DSS)-treated animals, as a model of Inflammatory Bowel Disease (see Sec. 2). As shown in Fig. 5, not only macroscopic aspects such as colon length (note the reduced length of the DSS colon in Fig. 5(a) compared with the healthy colon in Fig. 3(a)), but also alterations at a microscopic level (such as disruption of the villus structure) can be observed in the 3D volume rendered images in Fig. 5(b) and 5(c). It is important to note that these observations provide information on the development and severity of the disease by studying the intact 3D structure of the entire organ. This evaluation was previously only partly possible by histological analysis of successive microtome slices of small portions of tissue or by imaging tissue segments [12,41]. Here we demonstrate that the use of hOPT represents an efficient alternative to such analysis allowing the visualization of the entire sample and therefore providing unique information not possible to obtain otherwise.

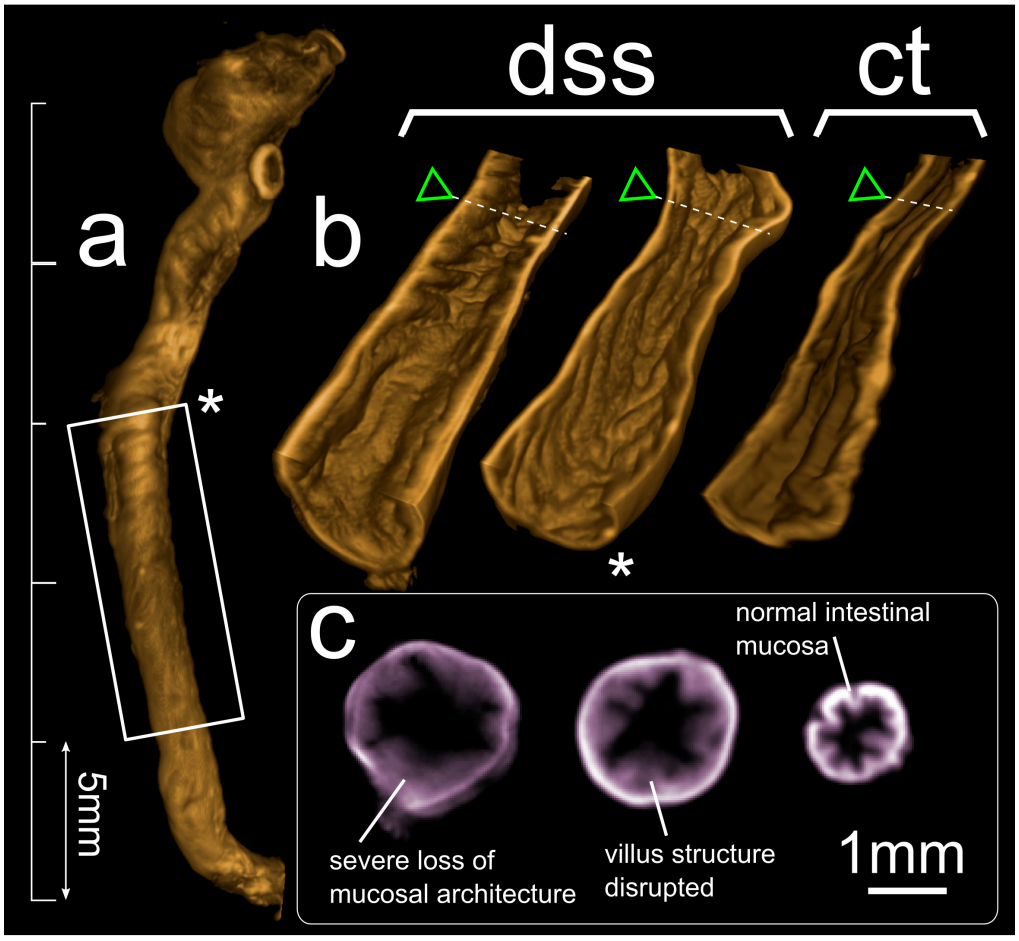

Fig. 5. The DSS model of colitis was established in C57BL/6 mice. Colons were obtained from healthy and DSS-treated animals and samples were prepared and imaged as described in Materials and Methods (Section 2). a) Volume render of a whole mouse colon from a DSS treated animal and (b) open volume renders of two DSS (asterisks indicate same colon sample) and one healthy (ct - control) mouse colon, including coronal slices of the area marked with the green arrowheads in (c). Tissue alteration in the inflamed mouse colon due to disruption of the villus structure can be observed in the 3D reconstructed data.

#193656 - $15.00 USD Received 10 Jul 2013; revised 5 Sep 2013; accepted 9 Sep 2013; published 23 Oct 2013

4. Discussion

The increasing interest in the development of new 3D optical imaging techniques is a response to the clear need to visualize structures otherwise difficult or even impossible to follow. In this work we presented hOPT, a new contribution to this emerging set of new 3D-optical technologies. Based on OPT, a widely tried and tested method, hOPT goes several steps further by eliminating the sample length limitation suffered by regular OPT additionally minimizing light exposure. Moreover, its experimental geometry makes the addition of a SPIM arm straightforward, providing the possibility of delivering high resolution images of the areas of interest combined with complete volumetric information.

One of the main disadvantages of current OPT setups is that images are acquired after the step-wise movement of the rotation stage, in what can be termed as a move-and-acquire approach. This approach results in longer experimental times. As described above, this drawback is solved in hOPT by incorporating in each saved image the complete information of the positions of all the stages (one for rotation and three for translation). In this way, hOPT enables the use of video-rate imaging and greatly reduces the time needed for each complete imaging session. By vertically translating the sample while recording images sequentially, we also reduce significantly the risk of photobleaching our samples unnecessarily. In doing so, we also expose the entire sample's volume to the same amount of light, rendering quantitative 3D images. As an example, our numerical simulations showed that imaging a homogeneous fluorescent cylinder of 4mm in diameter and 80mm in length, having the complete sample evenly exposed to light, would require an increase in the acquisition time of 1.87 fold when using stitched-OPT compared to hOPT. Moreover and for this same reason, the reconstruction times required to obtain the 3D-images of the same sample are significantly reduced when using hOPT instead of stitched-OPT.

Furthermore, in this paper we have first tested our hOPT system by successfully imaging cleared and fixed long tissue samples such as colons, pieces of small intestines and spinal cords from healthy control mice. The 3D images obtained with hOPT provided essential information to discriminate tissue alterations in large tissue sections of inflamed murine colons.

Overall, these results highlighted hOPT as a useful and attractive tool for biomedical applications, specifically those dealing with long samples.

5. Conclusion

We described here hOPT, an original adaptation of OPT that opens the door to new biomedical applications enabling 3D optical imaging of very long samples *in-toto*, which previously had to be imaged in sections. By imaging with hOPT instead of stitching several OPT sections the amount of light exposure of the sample is significantly reduced and so is the risk of photobleaching since hOPT ensures the same light exposure for the whole volume of the sample.

In summary, since hOPT does not require overlapping and stitching, we effectively reduce: the time required per experiment; the reconstruction times per sample; the inhomogeneous illumination; and most importantly, the total amount of light the sample receives.

Author Contributions

A.A and J.R. conceived and designed the project and performed the measurements; JR assembled the instrumentation and developed the instrument software control; A.A. prepared the samples; D.D. and S.Z. developed the reconstruction software with supervision from J.T.; D.D. performed the hOPT simulation; C.T. provided the DSS samples; M.R. provided consultation and reagents; A.A. and J.R. wrote the paper and designed the figures.

#193656 - $15.00 USD Received 10 Jul 2013; revised 5 Sep 2013; accepted 9 Sep 2013; published 23 Oct 2013

Acknowledgments

The authors would like to thank Prof. C. Mamalaki for constructive discussion and constant help while preparing the samples, Dr. A. Schroeter for assistance while obtaining spinal cord samples, and Dr. C. Lapointe for constructive comments on the manuscript. This work was partially supported by EC FP7 collaborative grant FMT-XCT and the Bill and Melinda Gates foundation. A.A. wishes to acknowledge support from Marie Curie IEF-2010-275137. J.R. wishes to acknowledge support from EC FP7 IMI project PREDICT-TB, and the EC FP7 CIG grant HIGH-THROUGHPUT TOMO. D.D., S.Z. and J.T. acknowledge support from the National Basic Research Program of China (973 Program) under Grant 2011CB707700, the Fellowship for Young International Scientists of the Chinese Academy of Sciences under Grant 2010Y2GA03, the National Natural Science Foundation of China under Grant 81101084 and Instrument Developing Project of the Chinese Academy of Sciences under Grant No. YZ201164.

#193656 - $15.00 USD Received 10 Jul 2013; revised 5 Sep 2013; accepted 9 Sep 2013; published 23 Oct 2013